

Development and Verification of the Three-Dimensional Electrostatic Particle Simulation Code for the Study of Blob and Hole Propagation Dynamics^{*)}

Hiroki HASEGAWA^{1,2)} and Seiji ISHIGURO^{1,2)}

¹⁾National Institute for Fusion Science (NIFS), National Institutes of Natural Sciences (NINS), Toki 509-5292, Japan

²⁾Department of Fusion Science, SOKENDAI (The Graduate University for Advanced Studies), Toki 509-5292, Japan

(Received 31 May 2017 / Accepted 28 September 2017)

The three-dimensional (3D) electrostatic particle-in-cell (PIC) simulation code for the study of blob and hole propagation dynamics has been developed and verified. The developed 3D-PIC code simulates the boundary layer plasma of magnetic confinement devices, and plasma particles in the simulation systems are distributed to form the blob or hole structures. For the verification, the theoretical blob and hole propagation speeds have been estimated, and the observed blob and hole propagation speeds in the simulations have been compared with the estimations. The observed relations between the propagation speed and the structure size in the blob and hole cases are in good agreement with the theoretical relations. The 3D-PIC code has reproduced a larger distortion of a hole shape than that of a blob shape. Furthermore, the code has shown that the propagation of a blob or a hole is faster without end plates. Such a situation is similar to the detached state.

© 2017 The Japan Society of Plasma Science and Nuclear Fusion Research

Keywords: blob, hole, scrape-off layer transport, particle-in-cell simulation

DOI: 10.1585/pfr.12.1401044

1. Introduction

The blob and the hole, which are intermittent filamentary coherent structures along the magnetic field line, are universally observed in the boundary layer plasmas of various magnetic confinement devices [1, 2]. Such structures are considered to play an important role in the radial transport in the boundary layer plasmas. The width of such structures is considered to be in meso-scale. In other words, the width of a small blob or a small hole is slightly larger than the ion Larmor radius. The microscopic, that is, the kinetic effects on blob and hole dynamics should be investigated because of such situations. Thus, we developed the three-dimensional (3D) electrostatic particle-in-cell (PIC) simulation code called “p3bd” (particle-in-cell 3-dimensional simulation code for boundary layer plasma dynamics) in order to study the kinetic effects on blob dynamics [3–5]. Since the sheath potential in the vicinity of the end plate or the wall is reproduced in the p3bd code, we are able to investigate the sheath effects on blob dynamics by using the code. In this study, we have updated the p3bd code in order to investigate the dynamics of hole (holes are thought to transport impurity ions [6–8]) and we have verified the code by comparison with the theoretical estimation of blob and hole dynamics. In Sec. 2, we briefly describe the simulation methodology. In Sec. 3, we derive the theoretical estimation of blob and hole propagation dy-

namics from the fluid model. In Sec. 4, we show the blob and hole dynamics simulated by the p3bd code and compare simulation results with the theoretical estimation. We summarize our work in Sec. 5.

2. Particle Simulation Code

The p3bd code is the electrostatic 3D-PIC code for the study of boundary layer plasma dynamics. In the code, the full plasma particle (electron and ions) dynamics (including the Larmor gyration motion) are calculated in 3D space and 3D velocity coordinates for all particles with the equations of motion,

$$\frac{d\mathbf{v}_{s,j}}{dt} = \frac{q_s}{m_s} [\mathbf{E}(\mathbf{x}_{s,j}) + \mathbf{v}_{s,j} \times \mathbf{B}(\mathbf{x}_{s,j})], \quad (1)$$

and

$$\frac{d\mathbf{x}_{s,j}}{dt} = \mathbf{v}_{s,j}, \quad (2)$$

where $\mathbf{x}_{s,j}$ is a position of a particle in 3D space, $\mathbf{v}_{s,j}$ is a 3D velocity of a particle, the subscripts s and j represent the species of a particle and the number of a particle, respectively, q_s and m_s are the charge and mass of species s , and $\mathbf{E}(\mathbf{x}_{s,j})$ and $\mathbf{B}(\mathbf{x}_{s,j})$ are the electric and magnetic fields on the particle position. Here, the value of a particle position has a real (continuous) number (not a discrete number).

As shown in Ref. [9], after particles are accelerated by Eq. (1) and moved by Eq. (2), the charge density ρ on each discrete spatial grid point is calculated from the positions

author's e-mail: hasegawa.hiroki@nifs.ac.jp

^{*)} This article is based on the invited talk at the 33rd JSPF Annual Meeting (2016, Tohoku)

of all particles by the charge assignment as

$$n_s(\mathbf{x}_{\alpha,\beta,\gamma}) = \sum_j S(\mathbf{x}_{s,j} - \mathbf{x}_{\alpha,\beta,\gamma}), \quad (3)$$

and

$$\varrho(\mathbf{x}_{\alpha,\beta,\gamma}) = \sum_s q_s n_s(\mathbf{x}_{\alpha,\beta,\gamma}), \quad (4)$$

in PIC simulation codes. Here, n_s is the density, $\mathbf{x}_{\alpha,\beta,\gamma}$ is the position of the grid whose numbers in the x , y , and z directions are α , β , and γ , and S is the form-factor of the finite-size particle. Then, the electric potential φ is solved with Poisson's equation,

$$\nabla^2 \varphi = -\frac{\varrho}{\varepsilon_0}, \quad (5)$$

by the fast Fourier transform (FFT) [10] where ε_0 is the permittivity. Here, the magnetic field is constant in time because of the electrostatic code. After the electric field on the discrete grid points is obtained from φ , the force at the particles seen in the right hand side of Eq. (1) is calculated from the fields on the grid points, $\mathbf{E}(\mathbf{x}_{\alpha,\beta,\gamma})$ and $\mathbf{B}(\mathbf{x}_{\alpha,\beta,\gamma})$, by the interpolation.

Although we are able to provide an arbitrary spatial profile for an external magnetic field \mathbf{B} in the p3bd code, it is assumed that \mathbf{B} is parallel to the z direction as shown in Fig. 1 and that the strength of \mathbf{B} is set as

$$B(x) = \frac{2L_x B_{Lx}}{3L_x - x}, \quad (6)$$

that is, $\partial B/\partial x > 0$, in this study. Here, L_x , L_y , and L_z are the system size in the x , y , and z directions and B_{Lx} is the magnetic field strength at $x = L_x$. Thus, the $-x$, y , and z directions correspond to the radial, poloidal, and toroidal

directions, respectively.

On the boundaries at $x = 0$ (corresponding to the vessel wall) and both edges in the z direction (corresponding to the end plates) displayed as shaded plates in Fig. 1, plasma particles are absorbed and the electric potential is fixed as $\varphi = 0$. In the simulations, the sheath potential is formed self-consistently near edges in the z direction without any artificial methods (e.g., a logical sheath) since the grid size satisfies $\Delta_g = \lambda_D$, where λ_D is the Debye length. Some low energy electrons are reflected by the sheath potential and it is observed that the net current to the sheath is nearly equal to zero outside of the blob or the hole region. (In the higher or lower potential side in the blob or the hole region, the net current in the z direction becomes $\sim enc_s$ [5], where n and c_s are the plasma density and the ion acoustic speed.) On the other hand, a periodic boundary condition is applied in the y direction. On the plane at $x = L_x$, plasma particles are reflected and the electric potential satisfies $\partial\varphi/\partial x = 0$.

A blob or a hole is initially provided as a cylindrical form elongated between both edges in the z direction. That is, the electron and ion particles in a blob and in background plasma are initially distributed by

$$n_{s,\text{init}}(x, y) = n_{\text{sf0}} \left[1 + \hat{n}_{\text{b0}} g_x(x) g_y(y) \right], \quad (7)$$

or the electron and ion particles in a hole and in background plasma are initially distributed by

$$n_{s,\text{init}}(x, y) = n_{\text{sf0}} \left[1 - \hat{n}_{\text{b0}} g_x(x) g_y(y) \right], \quad (8)$$

where n_{sf0} is the initial density of background plasma which satisfies

$$\sum_s q_s n_{\text{sf0}} = 0, \quad (9)$$

\hat{n}_{b0} is the ratio between the initial density amplitude of the blob or the hole and background plasma density, g_x and g_y are defined by

$$g_x(x) = \exp\left(-\frac{(x - x_{\text{b0}})^2}{2\delta_{\text{bx}}^2}\right), \quad (10)$$

and

$$g_y(y) = \exp\left(-\frac{(y - y_{\text{b0}})^2}{2\delta_{\text{by}}^2}\right), \quad (11)$$

respectively. $(x_{\text{b0}}, y_{\text{b0}})$ is the initial position of the center of a blob or a hole, and δ_{bx} and δ_{by} are the blob or hole widths in the x and y directions. Equations (7), (8), (10), and (11) show that the blob or the hole is initially located along the ambient magnetic field around $(x_{\text{b0}}, y_{\text{b0}})$.

In the blob case, the p3bd code first distributes the particles of background plasma uniformly in the 3D space by using random numbers. Secondly, the particles of a blob are distributed by using random numbers and the inversions of the one-dimensional (1D) cumulative distribution

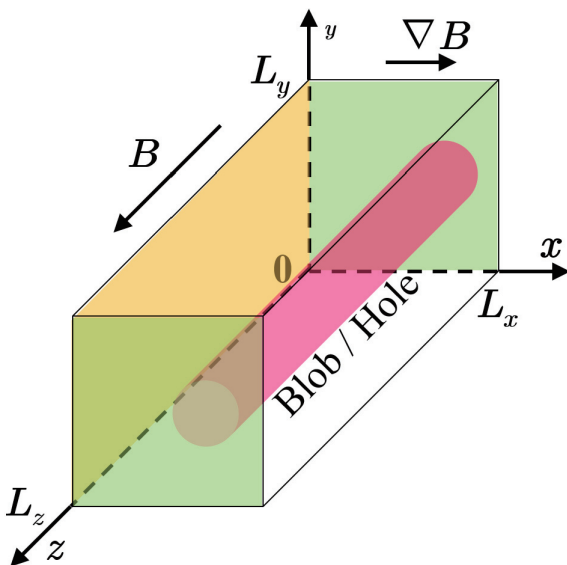


Fig. 1 Schematic diagram of the simulation configuration. The simulation system reproduces the boundary layer of magnetic confinement devices.

functions, where the 1D cumulative distribution functions are given by

$$G_{bx}(x) = \frac{\int_0^x g_x(\tilde{x}) d\tilde{x}}{\int_0^{L_x} g_x(\tilde{x}) d\tilde{x}}, \quad (12)$$

and

$$G_{by}(y) = \frac{\int_0^y g_y(\tilde{y}) d\tilde{y}}{\int_0^{L_y} g_y(\tilde{y}) d\tilde{y}}. \quad (13)$$

In the hole case, we cannot apply the same method as that in the blob case, i.e., using the 1D cumulative distribution functions, because the density profiles as a dug hole cannot be given by superimposing the inversions of the 1D cumulative distribution functions. Thus, we have developed a new method which uses the two-dimensional (2D) cumulative distribution function. The initial density equation, Eq. (8), is separated into

$$n_{s,init1} = n_{sf0}(1 - \hat{n}_{b0}), \quad (14)$$

and

$$n_{s,init2}(x, y) = n_{sf0} \hat{n}_{b0} [1 - g_x(x) g_y(y)]. \quad (15)$$

The code first distributes the particles of the first part described by Eq. (14) uniformly in the 3D space by using random numbers. Secondly, the particles of the second part described by Eq. (15) are distributed by using random numbers and the inversion of the 2D cumulative distribution function, where the 2D cumulative distribution function is given by

$$G_h(x, y) = \frac{\int_0^y \int_0^x [1 - g_x(\tilde{x}) g_y(\tilde{y})] d\tilde{x} d\tilde{y}}{\int_0^{L_y} \int_0^{L_x} [1 - g_x(\tilde{x}) g_y(\tilde{y})] d\tilde{x} d\tilde{y}}. \quad (16)$$

Actually, the code calculates the 2D cumulative distribution function by

$$G_h(i) = \frac{\sum_{j=1}^i [1 - g_x(\tilde{x}_j) g_y(\tilde{y}_j)] \Delta x \Delta y}{\sum_{j=1}^{M_x M_y} [1 - g_x(\tilde{x}_j) g_y(\tilde{y}_j)] \Delta x \Delta y}, \quad (17)$$

where

$$x_j = \Delta x [j - M_x \text{int}(j/M_x) - 0.5], \quad (18)$$

$$y_j = \Delta y [\text{int}(j/M_x) + 0.5], \quad (19)$$

i and j are integer numbers, and M_x and M_y are also the integer numbers defined by $M_x = L_x/\Delta x$ and $M_y = L_y/\Delta y$. Since Eqs. (17)–(19) provide the discrete positions in the y direction to particles, the positions in the y direction are obtained from the discrete positions given by Eqs. (17)–(19) by the linear interpolation and random numbers.

The simulation system of the p3bd code does not have

particle and heat sources. Although the density distribution does not satisfy equilibrium with the magnetic field as seen in Eqs. (6), (7), and (8) and the temporal evolution of the magnetic field is not solved, as mentioned above, such assumptions are appropriate in the low beta limit.

3. Blob and Hole Dynamics

We now consider the theoretical estimation of blob and hole propagation dynamics on the basis of the simple fluid model. The blob and hole dynamics are described by the equation for the charge conservation [1],

$$\nabla_{\perp} \cdot \mathbf{j}_{\perp} + \nabla_{\parallel} j_{\parallel} = 0, \quad (20)$$

where \mathbf{j}_{\perp} and j_{\parallel} are the currents perpendicular and parallel to the magnetic field. The perpendicular current, \mathbf{j}_{\perp} , includes the currents caused by the polarization and grad- B drifts, i.e.,

$$\mathbf{j}_{\perp} = \mathbf{j}_p + \mathbf{j}_g, \quad (21)$$

where the polarization drift current and the grad- B drift current are given by

$$\mathbf{j}_p = - \left(\sum_s n_s m_s \right) \frac{1}{B^2} \frac{D(\nabla_{\perp} \phi)}{Dt}, \quad (22)$$

and

$$\mathbf{j}_g = \left(\sum_s n_s T_s \right) \frac{1}{B^2} \frac{\partial B \mathbf{y}}{\partial x y}, \quad (23)$$

respectively. Here, D/Dt represents the Lagrangian derivative defined by $\partial/\partial t + \mathbf{v}_{E \times B} \cdot \nabla$, $\mathbf{v}_{E \times B}$ is the $E \times B$ drift velocity, T_s is the initial temperature, and we assume that \mathbf{B} is parallel to the z direction and that $B (= |\mathbf{B}|)$ depends upon only x .

3.1 Sheath-limited case

In the case where the parallel current, j_{\parallel} , is limited by the sheath formed on the end plates, the divergence of the parallel current is given by the following equation [11],

$$\begin{aligned} \nabla_{\parallel} j_{\parallel} &= \frac{j_{\parallel, Lz} - j_{\parallel, 0}}{L_z} \\ &= \frac{2 j_{\parallel, Lz}}{L_z} \\ &= \frac{2}{L_z} \left[\sum_s q_s n_{s, Lz} v_{zs, Lz} \right] \\ &= \frac{2 n_{em} e c_{si}}{L_z} \left[\left(\sum_l \frac{n_{lm} q_l c_{sl}}{n_{em} e c_{si}} \sqrt{1 + \frac{T_l}{T_e}} \right) \right. \\ &\quad \left. - \sqrt{\frac{m_i}{2\pi m_e}} \exp\left(-\frac{e\phi}{T_e}\right) \right], \quad (24) \end{aligned}$$

where $j_{\parallel, 0}$ and $j_{\parallel, Lz}$ are the parallel currents at $z = 0$ and L_z , i.e., at both end plates, $n_{s, Lz}$ and $v_{zs, Lz}$ are the density and the parallel flow velocity at $z = L_z$, n_{sm} is the density of the main plasma not including the sheath, e is the elementary charge, c_{sl} is the ion acoustic speed given by

$c_{sl} = (T_e/m_l)^{1/2}$, ϕ is the electric potential in the main plasma, and the subscripts e, i, and l represent the electron, the major ion, and a species of ions (including the major ion), respectively. In the derivation of Eq. (24), we assume that $q_e = -e$ and use the relations, $n_{l,Lz} = n_{lm}$, $v_{zl,Lz} = c_{sl} (1 + T_l/T_e)^{1/2}$, $n_{e,Lz} = n_{em} \exp(-e\phi/T_e)$, and $v_{ze,Lz} = v_{Te}/\sqrt{2\pi}$, where v_{Ts} is the initial thermal velocity.

Using Eqs. (22)–(24) and assuming that $D/Dt = 0$ and that $n_{lm} = n_{em}(n_{lf0}/n_{ef0})$, Eq. (20) becomes

$$\begin{aligned}
 c_{si} \left(1 + \sum_l \frac{n_{lf0}}{n_{ef0}} \frac{T_l}{T_e} \right) \frac{m_i}{B^2} \frac{\partial B}{\partial x} \frac{\partial(\ln n_{em})}{\partial y} \\
 + \frac{2e}{L_z} \left[\left(\sum_l \frac{n_{lf0}}{n_{ef0}} \frac{q_l c_{sl}}{e c_{si}} \sqrt{1 + \frac{T_l}{T_e}} \right) \right. \\
 \left. - \sqrt{\frac{m_i}{2\pi m_e}} \exp\left(-\frac{e\phi}{T_e}\right) \right] = 0, \quad (25)
 \end{aligned}$$

where n_{sm} is substituted for n_s in Eq. (23). Since the propagation speed of a blob or a hole is given by the x component of $\mathbf{v}_{E \times B}$, that is, $-(\partial\phi/\partial y)/B$, the derivative of Eq. (25) regarding y provides the propagation speed v_b as

$$\frac{v_b}{c_{si}} = \frac{1}{2} A_{sh} L_z \rho_{si}^2 \frac{B_{Lx}^2}{B^3} \frac{\partial B}{\partial x} \frac{\partial^2(\ln n_{em})}{\partial y^2}, \quad (26)$$

where A_{sh} and ρ_{si} are defined by

$$A_{sh} = \frac{q_i^2}{e^2} \left(1 + \sum_l \frac{n_{lf0}}{n_{ef0}} \frac{T_l}{T_e} \right) \sqrt{\frac{2\pi m_e}{m_i}} \exp\left(\frac{e\phi}{T_e}\right), \quad (27)$$

and $\rho_{si} = c_{si}/\Omega_i$, respectively, and Ω_i is the cyclotron frequency of the major ion at $x = L_x$.

Substituting Eqs. (6) and (7) for B and n_{em} in Eq. (26), respectively, we obtain v_b in this study as

$$\begin{aligned}
 \frac{v_b}{c_{si}} = & -\frac{A_{sh} L_z}{8L_x} \left(3 - \frac{x}{L_x} \right) \left(1 - \frac{n_{ef0}}{n_{e,init}(x,y)} \right) \\
 & \times \left[1 - \frac{n_{ef0}}{n_{e,init}(x,y)} \frac{(y - y_{b0})^2}{\delta_{by}^2} \right] \frac{\rho_{si}^2}{\delta_{by}^2}. \quad (28)
 \end{aligned}$$

(Even if we substitute Eq. (8) for n_{em} , Eq. (28) is derived. That is, v_b for the hole case is given by the same equation as that for the blob case.) Equation (28) indicates that a blob or a hole propagates in the $\mp \nabla B$ direction and that the propagation speed is proportional to δ_{by}^{-2} . Furthermore, it is obvious that the shear term in Eq. (28), i.e., the term including $(y - y_{b0})^2$, will become larger in the hole case than the shear term in the blob case because $\hat{n}_{b0} < 1$ in the hole case although \hat{n}_{b0} is not restricted in the blob case [6].

3.2 Periodic boundary case

In this section, we now consider the case without the end plates, that is, with the periodic boundary condition applied in the z direction. This situation is called the ‘‘inertial’’ case in previous papers [1] because the dynamics are determined by the inertial term in the model equation rather than by the sheath term. In this case, the divergence of the parallel current is given by

$$\nabla_{\parallel} j_{\parallel} = 0, \quad (29)$$

with the assumption that the dynamics are independent of z . Therefore, Eq. (20) becomes

$$\frac{B}{B} \cdot \left[\frac{D}{Dt} (\nabla_{\perp} \times \mathbf{v}_{E \times B}) \right] = A_{pr} c_{si}^2 \frac{\partial(\ln B)}{\partial x} \frac{\partial(\ln n_e)}{\partial y}, \quad (30)$$

where the Boussinesq approximation is used. It is assumed that $n_l = n_e(n_{lf0}/n_{ef0})$. A_{pr} is defined by

$$A_{pr} = \frac{1 + \sum_l \frac{n_{lf0}}{n_{ef0}} \frac{T_l}{T_e}}{\sum_s \frac{n_{sf0}}{n_{ef0}} \frac{m_s}{m_i}}. \quad (31)$$

Furthermore, we use the electron continuity equation,

$$\begin{aligned}
 \frac{Dn_e}{Dt} = & -\mathbf{v}_{ge} \cdot \nabla_{\perp} n_e - n_e \nabla_{\perp} \cdot (\mathbf{v}_{E \times B} + \mathbf{v}_{ge}) \\
 = & \frac{T_e}{eB^2} \frac{\partial B}{\partial x} \frac{\partial n_e}{\partial y} - n_e \nabla_{\perp} \cdot \mathbf{v}_{E \times B}, \quad (32)
 \end{aligned}$$

where \mathbf{v}_{ge} is the electron grad- B drift velocity. Linearizing Eqs. (30) and (32), we obtain the estimation of the blob or hole propagation speed [1, 12] as

$$v_b \approx c_{si} \left(A_{pr} \frac{\delta_{bx}}{B} \frac{\partial B}{\partial x} \right)^{1/2}. \quad (33)$$

In the derivation of Eq. (33), the y component of $\mathbf{v}_{E \times B}$ and the wave number in the y direction, $k_y \sim 1/\delta_{by}$, are neglected.

4. Simulation Results

We next show simulation results calculated by the p3bd code. In this section, results of blob and hole propagation simulations in both the sheath-limited and periodic boundary cases are presented and compared with the theoretical estimations.

The simulation parameters are as follows. The number of spatial cells contained in the simulation system is $N_x \times N_y \times N_z = 64 \times 64 \times 256$, where $N_x = L_x/\Delta_g$ and Δ_g is the grid spacing. The size of the grid spacing is set as $\Delta_g \approx 0.5 \rho_{si}$, as shown in Tables 1 and 2. The time step Δt is also found in these tables. We assume that the plasma is composed by two particle species, i.e., electron ($s = e$) and ion ($s = i$), whose masses and charges are set as $m_i/m_e = 100$ and $-q_e = q_i$. The initial ion-to-electron temperature ratio is $T_i/T_e = 0.01$. Thus, the initial ion-to-electron thermal velocity ratio is $v_{Ti}/v_{Te} = 0.01$ (we assume low ion temperature [i.e., small ion Larmor radius] in order to verify the code). Here, the initial temperature in the blob is equal to that of the background plasma and the initial velocity distribution is given by Maxwellian. There are 72 electrons and an equal number of ions per cell on average. The external magnetic field strength is given by $\Omega_i/\omega_{pi} = 0.5$ where ω_{pi} is the ion plasma frequency in the

Table 1 Parameters of blob propagation simulations.

Symbol (Sheath / Periodic)	Δ_g/ρ_{si}	$\Omega_i \Delta t$	δ_{bx}/ρ_{si}	δ_{by}/ρ_{si}
● / ○	0.488	1.22×10^{-3}	1.95	1.46
▲ / △	0.484	1.21×10^{-3}	1.94	1.94
■ / □	0.477	1.19×10^{-3}	1.91	2.86
▼ / ▽	0.470	1.17×10^{-3}	1.88	3.76
◆ / ◇	0.457	1.14×10^{-3}	1.83	5.48

Table 2 Parameters of hole propagation simulations.

Symbol (Sheath / Periodic)	Δ_g/ρ_{si}	$\Omega_i \Delta t$	δ_{bx}/ρ_{si}	δ_{by}/ρ_{si}
● / ○	0.503	1.26×10^{-3}	2.01	1.51
▲ / △	0.505	1.26×10^{-3}	2.02	2.02
■ / □	0.507	1.27×10^{-3}	2.03	3.04
▼ / ▽	0.509	1.27×10^{-3}	2.04	4.07
◆ / ◇	0.514	1.28×10^{-3}	2.06	6.17

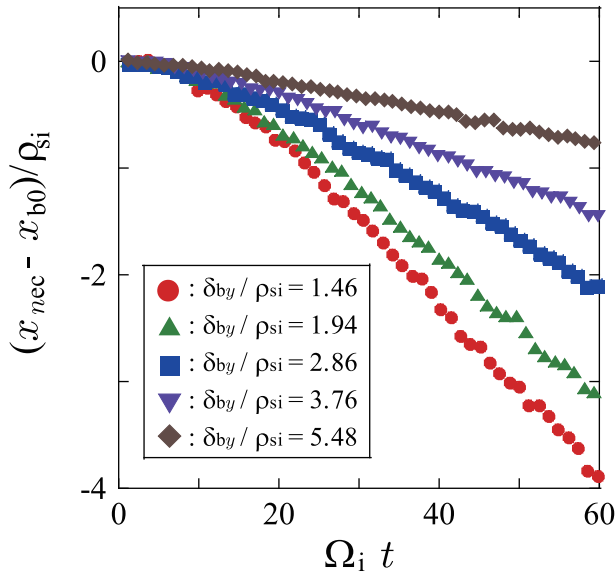


Fig. 2 Time variations of position of the electron center of mass in a blob, x_{nec} , on the x - y plane at $z = L_z/2$ in the sheath-limited case. The circles (●), triangles (▲), squares (■), inverse triangles (▼), and diamonds (◆) represent results of calculations shown in Table 1, respectively.

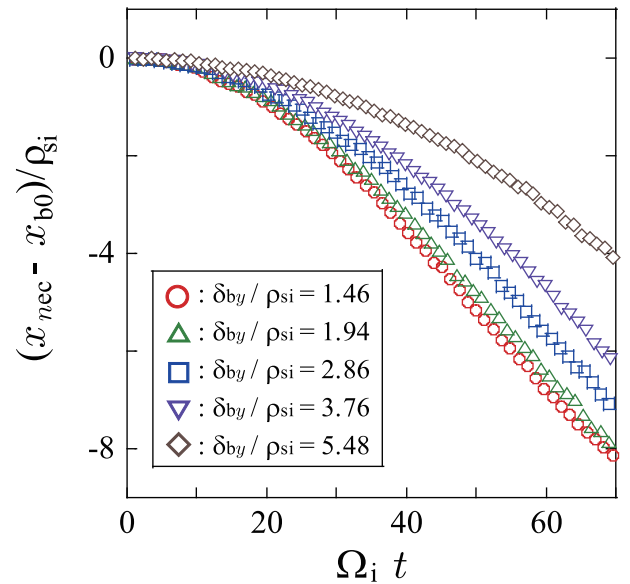


Fig. 3 Time variations of position of the electron center of mass in a blob, x_{nec} , on the x - y plane at $z = L_z/2$ in the periodic boundary case. The circles (○), triangles (△), squares (□), inverse triangles (▽), and diamonds (◇) represent results of calculations shown in Table 1, respectively.

initial background plasma. The initial density ratio of the blob to the background plasmas is $\hat{n}_{b0} = 2.7$ in the blob case. On the other hand, the initial density ratio between the center of the hole and the background plasma is set as $1 - \hat{n}_{b0} = 0.27$ in the hole case. The initial blob width or hole width in the radial direction is $\delta_{bx} = 4\Delta_g \approx 2\rho_{si}$. The initial poloidal width of a structure is given by $\delta_{by}/\Delta_g = 3, 4, 6, 8,$ or 12 as seen in Tables 1 and 2. The initial positions of the blob and the hole are $(x_{b0}, y_{b0}) = (3L_x/4, L_y/2)$ and $(L_x/2, L_y/2)$, respectively.

In Figs. 2 and 3, we show the results of blob propaga-

tion simulations. Figures 2 and 3 represent the time variations of the x component of the position of the electron center of mass, x_{nec} , on the x - y plane at $z = L_z/2$ in the sheath-limited and periodic boundary cases, respectively. Here, x_{nec} is obtained in the area in which the electron density, n_e , is higher than $n_{ef} (1 + \hat{n}_{b0}/10)$, where n_{ef} is calculated by $[\int_0^{L_y} n_e(x \approx L_x, y, z = L_z/2) dy] / L_y$. Since x_{nec} represents a blob position, we obtain the blob propagation speeds in each simulation from the data of x_{nec} between $\Omega_i t = 20$ and 60 (the sheath-limited case shown in Fig. 2) or $\Omega_i t = 40$ and 70 (the periodic boundary case shown

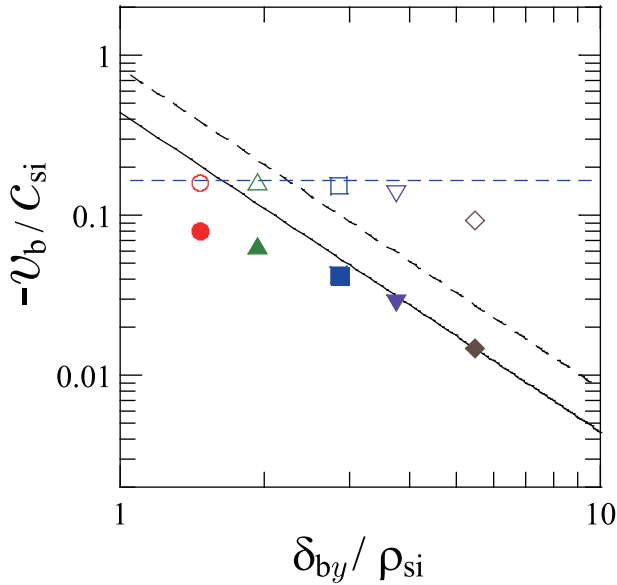


Fig. 4 Relation between the poloidal blob size, δ_{by} , and the blob radial propagation speed, v_b . The solid and open symbols represent the observed propagation speeds in the calculations with the parameters shown in Table 1 in the sheath-limited and periodic boundary cases, respectively. The black solid and broken lines show the theoretical average and maximum speeds in the sheath-limited case. Also, the blue broken line presents the theoretical speed in the periodic boundary case.

in Fig. 3). We show the relation between the poloidal blob width, δ_{by} , and the blob propagation speed in the radial direction, v_b , in Fig. 4. In this figure, the black lines and the blue broken line represent the theoretical speeds in the sheath-limited and periodic boundary cases given by Eqs. (28) and (33), respectively. In the computation of these theoretical speeds, we use the initial parameters shown above and assume that the potential in A_{sh} described by Eq. (27) is given by

$$\frac{e\phi}{T_e} = \frac{1}{2} \ln \left(\frac{m_i}{2\pi m_e (1 + T_i/T_e)} \right), \quad (34)$$

which is obtained from the condition in which the net current to the sheath is zero, that is, $n_{e,Lz} v_{ze,Lz} = n_{i,Lz} v_{zi,Lz}$. The black solid line designates the average speed and the black broken line designates the maximum speed, where the average speeds are calculated by

$$\langle v_b \rangle = \frac{\iint_{\sigma} v_b(x, y) g_x(x) g_y(y) dx dy}{\iint_{\sigma} g_x(x) g_y(y) dx dy}, \quad (35)$$

σ is the area defined by

$$\frac{(x - x_{b0})^2}{2\delta_{bx}^2} + \frac{(y - y_{b0})^2}{2\delta_{by}^2} \leq \ln(10), \quad (36)$$

and the maximum speeds are obtained by substituting (x_{b0}, y_{b0}) for (x, y) in Eq. (28).

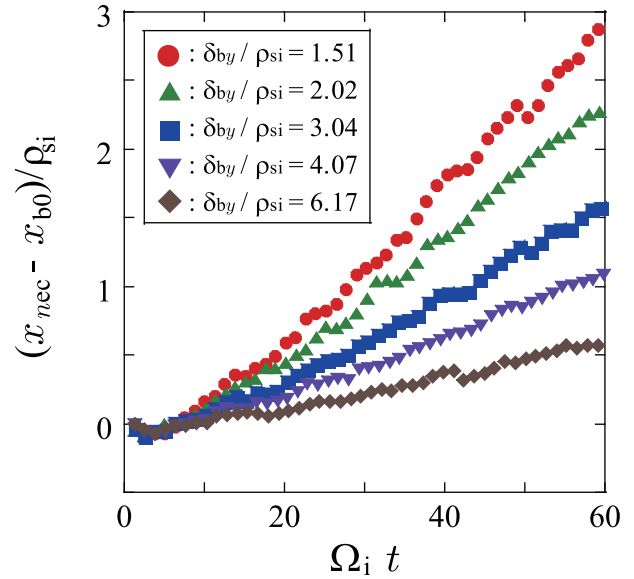


Fig. 5 Time variations of position of the electron center of mass in a hole, x_{nec} , on the x - y plane at $z = L_z/2$ in the sheath-limited case. The circles (\bullet), triangles (\blacktriangle), squares (\blacksquare), inverse triangles (\blacktriangledown), and diamonds (\blacklozenge) represent results of calculations shown in Table 2, respectively.

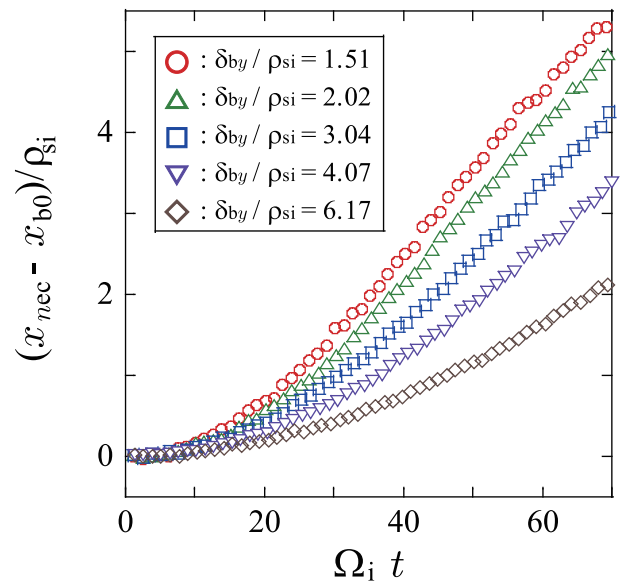


Fig. 6 Time variations of position of the electron center of mass in a hole, x_{nec} , on the x - y plane at $z = L_z/2$ in the periodic boundary case. The circles (\circ), triangles (\triangle), squares (\square), inverse triangles (∇), and diamonds (\diamond) represent results of calculations shown in Table 2, respectively.

On the other hand, we show the results of hole propagation simulations in Figs. 5 and 6 which represent the time variations of x_{nec} on the x - y plane at $z = L_z/2$ in the sheath-limited and periodic boundary cases, respectively. Here, x_{nec} is calculated by

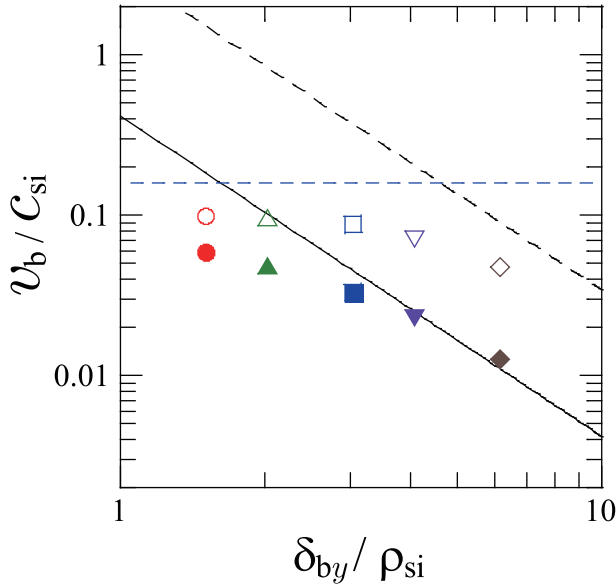


Fig. 7 Relation between the poloidal hole size, δ_{by} , and the hole radial propagation speed, v_b . The solid and open symbols represent the observed propagation speeds in the calculations with the parameters shown in Table 2 in the sheath-limited and periodic boundary cases, respectively. The black solid and broken lines show the theoretical average and maximum speeds in the sheath-limited case. Also, the blue broken line presents the theoretical speed in the periodic boundary case.

$$x_{nec} = \frac{\iint_H x [n_{ef} (1 - \hat{n}_{b0}/10) - n_e(x, y)] dx dy}{\iint_H [n_{ef} (1 - \hat{n}_{b0}/10) - n_e(x, y)] dx dy}, \quad (37)$$

where H is the area in which the electron density, n_e , is lower than $n_{ef}(1 - \hat{n}_{b0}/10)$ and n_{ef} is calculated by the same process as that mentioned above. Also, we obtain the hole propagation speeds in each simulation from the data of x_{nec} between $\Omega_i t = 20$ and 60 (the sheath-limited case shown in Fig. 5) or $\Omega_i t = 40$ and 70 (the periodic boundary case shown in Fig. 6). Figure 7 shows the relation between the poloidal hole width, δ_{by} , and the hole propagation speed in the radial direction, v_b . The black lines and the blue broken line in this figure represent the theoretical speeds in the sheath-limited and periodic boundary cases given by Eqs. (28) and (33), respectively. In the computation of these theoretical speeds, we use the initial parameters shown above and assume that the potential in A_{sh} described by Eq. (27) is given by Eq. (34). The black solid line designates the average speed and the black broken line designates the maximum speed, where the average and maximum speeds are obtained by the same calculations as those shown above.

Figures 4 and 7 indicate that the observed propagation speeds are in agreement with the theoretical estimation. In the sheath-limited case, the observed propagation speeds

of small blobs and holes are slower than the theoretical estimation, which is thought to arise from kinetic effects because of the approach of structure size to the ion Larmor radius or from some instabilities because the poloidal width δ_{by} of such blobs is smaller than $\delta_* \sim \rho_{si} [L_z^2 / (\rho_{si} L_x)]^{1/5}$, where δ_* is the particular width for the long distance propagation as shown by Eq. (17) in Ref. [1] and $\delta_* \sim 3\rho_{si}$ in this study. (In these sheath-limited case simulations, dynamics by instabilities [e.g., the evolution to mushroom shape] are not observed clearly because the calculation time is too short to observe such dynamics due to the small L_z .)

Figure 8 shows the time evolutions of the electron density distribution on the x - y plane at $z = L_z/2$ in the blob (a) and hole (b) propagations in the sheath-limited case. This figure indicates that the distortion of the hole shape is larger than that of the blob shape. The large distortion of the hole shape occurs by the velocity shear as mentioned in Sec. 3.1.

5. Summary and Discussion

We have developed, updated, and verified the electrostatic 3D-PIC simulation code for the study of blob and hole propagation dynamics, that is, the p3bd code. We are able to simulate the boundary layer plasma of magnetic confinement devices by the p3bd code. Although only a blob structure is initially provided in the simulation systems in the previous version of the p3bd code, the updated p3bd code is able to simulate the hole propagation. For the verification of the code, we have estimated the theoretical blob and hole propagation speeds and compared the observed blob and hole propagation speeds in the simulations with the theoretical estimations. The observed relations between the propagation speed and the structure size in both the blob and the hole cases are in good agreement with the theoretical relations. Also, the code has reproduced the large distortion of the hole shape by the velocity shear.

We plan to study effects of the kinetic dynamics and the sheath on the blob and hole dynamics and the dependence of the blob and hole dynamics on various parameters, for instance, the ion temperature, the localization of structure, the spatial profile of magnetic field, and other issues. Although the dependence of the structure dynamics on z is not observed in the simulations shown in this paper, the parallel dynamics including the effect of the parallel current of electrons [13, 14] will be also studied by the 3D-PIC code. Furthermore, we will investigate the effect of the impurity ion transports by the blob and hole propagations [7, 8] on the total transport by the p3bd code. We will apply additional collision models [15, 16] and detachment dynamics [17] to the p3bd code and optimize the code for large-scale simulations. These topics are also important in future work. In particular, detachment dynamics may be important on blob and hole dynamics because the enhancement of the radial plasma transport in the boundary

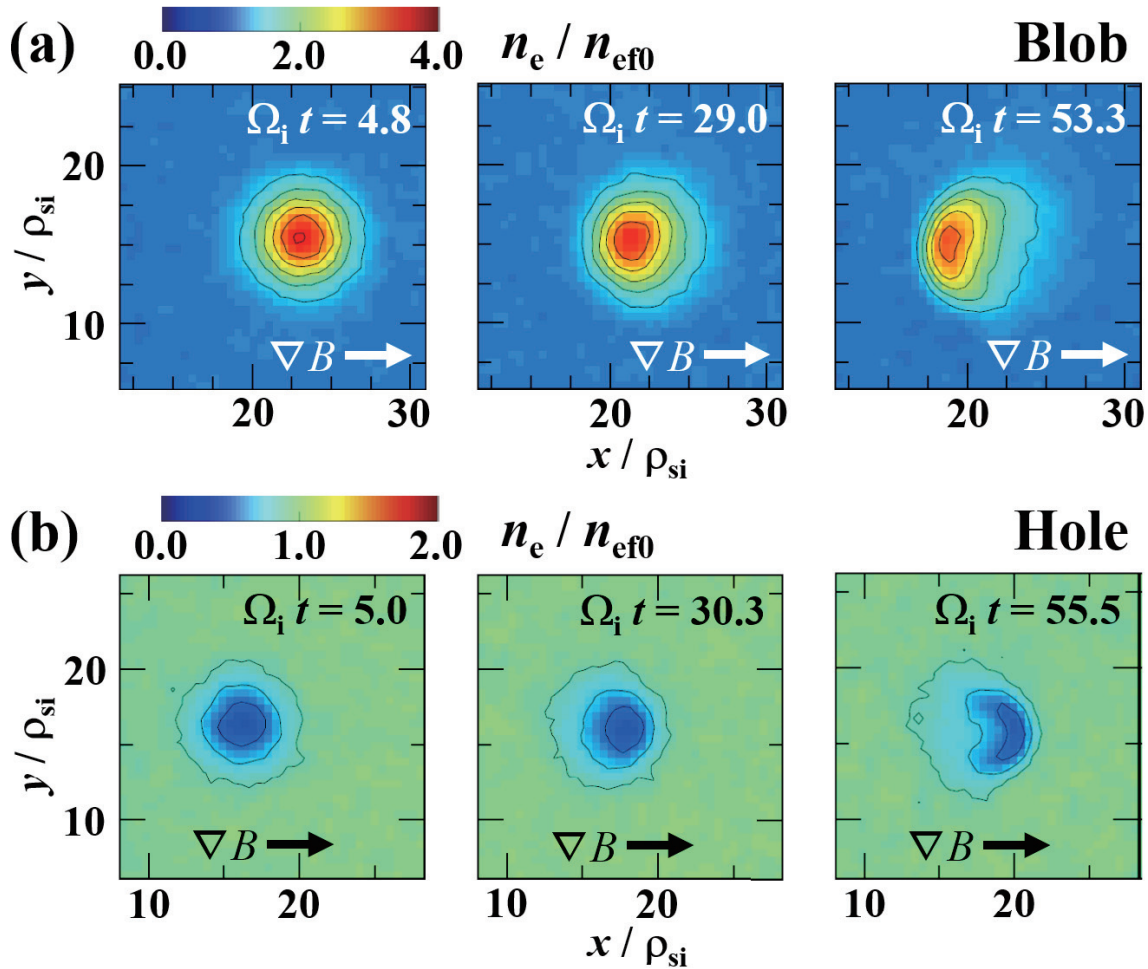


Fig. 8 Time evolutions of the electron density distribution on the x - y plane at $z = L_z/2$ in the blob (a) and hole (b) propagations in the sheath-limited case, where $\delta_{by}/\Delta_g = 4$. These simulations are represented by the triangle (\blacktriangle) in the above tables and figures.

layer during the detached state was observed in some experiments [18–21]. Although the electric field in a blob or a hole, namely, the radial propagation speed, is reduced by the short-circuit on the end plate in the attached state, the detached plasma might prevent the short-circuit. Actually, the simulations in this study show that the radial propagation speed of a blob or a hole without the short-circuit, i.e., in the periodic boundary case, is faster than that with the short-circuit, i.e., in the sheath-limited case, as seen in Figs. 4 and 7.

Acknowledgments

The simulations were carried out on the Plasma Simulator (PS) of the National Institute for Fusion Science (NIFS) and the high-performance computer system of Nagoya University. This work is performed with the support and under the auspices of the NIFS Collaboration Research programs (NIFS15KNSS058, NIFS14KNXN279, NIFS15KNSS039, NIFS15KNSS040, and NIFS16KNNTT038), supported by a Grant-in-Aid for Scientific Research from the Japan Society for the Promotion of Science (KAKENHI 23740411), and partially

supported by “Joint Usage/Research Center for Interdisciplinary Large-scale Information Infrastructures” and “High Performance Computing Infrastructure” in Japan (jh160023-NAH).

- [1] S.I. Krasheninnikov, D.A. D’Ippolito and J.R. Myra, *J. Plasma Phys.* **74**, 679 (2008) and references therein.
- [2] D.A. D’Ippolito, J.R. Myra and S.J. Zweben, *Phys. Plasmas* **18**, 060501 (2011) and references therein.
- [3] S. Ishiguro and H. Hasegawa, *J. Plasma Phys.* **72**, 1233 (2006).
- [4] H. Hasegawa and S. Ishiguro, *Plasma Fusion Res.* **7**, 2401060 (2012).
- [5] H. Hasegawa and S. Ishiguro, *Phys. Plasmas* **22**, 102113 (2015).
- [6] S.I. Krasheninnikov *et al.*, Proc. 19th IAEA Fusion Energy Conf. (Lyon, France, 2002) (International Atomic Energy Agency, Vienna, 2003) IAEA-CN-94/TH/4-1.
- [7] H. Hasegawa and S. Ishiguro, Proc. 26th IAEA Fusion Energy Conf. (Kyoto, Japan, 2016) (International Atomic Energy Agency, Vienna, 2017) IAEA-CN-234-0135/TH/P6-17.
- [8] H. Hasegawa and S. Ishiguro, *Nucl. Fusion* **57**, 116008 (2017).

- [9] C.K. Birdsall and A.B. Langdon, *Plasma Physics via Computer Simulation* (McGraw-Hill Book Company, New York, 1985, Institute of Physics Publishing, Bristol and Philadelphia, 1991, and Adam Hilger, Bristol and New York, 1991).
- [10] W.H. Press *et al.*, *Numerical recipes in Fortran 77 : The art of scientific computing, 2nd ed.* (Cambridge University Press, New York, 1996).
- [11] D.A. D'Ippolito, J.R. Myra and S.I. Krasheninnikov, *Phys. Plasmas* **9**, 222 (2002).
- [12] J.R. Myra and D.A. D'Ippolito, *Phys. Plasmas* **12**, 092511 (2005).
- [13] D. Jovanović, P.K. Shukla and F. Pegoraro, *Phys. Plasmas* **15**, 112305 (2008).
- [14] J.D. Angus, S.I. Krasheninnikov and M.V. Umansky, *Phys. Plasmas* **19**, 082312 (2012).
- [15] T. Takizuka and H. Abe, *J. Comput. Phys.* **25**, 205 (1977).
- [16] K. Nanbu, *Phys. Rev. E* **55**, 4642 (1997).
- [17] T. Pianpanit, S. Ishiguro and H. Hasegawa, *Plasma Fusion Res.* **11**, 2403040 (2016).
- [18] R. Décoste *et al.*, *Plasma Phys. Control. Fusion* **38**, A121 (1996).
- [19] B.L. Stansfield *et al.*, *J. Nucl. Mater.* **241-243**, 739 (1997).
- [20] N. Ohno, K. Furuta and S. Takamura, *J. Plasma Fusion Res.* **80**, 275 (2004).
- [21] H. Tanaka *et al.*, *Phys. Plasmas* **17**, 102509 (2010).